1 Revision 1

2 Phase Transitions and Equation of State of Forsterite to 90 GPa from Single-Crystal X-

3 Ray Diffraction and Molecular Modeling

4

5 Gregory J. Finkelstein[1]*, Przemyslaw K. Dera[2, 3], Sandro Jahn[4], Artem R. Oganov[5],

6 Christopher M. Holl[1], Yue Meng[6], and Thomas S. Duffy[1]

7

8 [1] Department of Geosciences, Princeton University, Princeton, NJ 08544, USA

9 [2] GSECARS, University of Chicago, Building 434A, 9700 South Cass Avenue, Argonne,

10 Illinois 60439, USA

11 [3] Hawaii Institute of Geophysics & Planetology, School of Ocean and Earth Science and

12 Technology, University of Hawaii, 1680 East West Road (POST Bldg 819E), Honolulu,

13 Hawaii 96822, USA

14 [4] GFZ German Research Centre for Geosciences, Telegrafenberg, 14473 Potsdam,

15 Germany

16 [5] Department of Geosciences and Department of Physics and Department of Physics and

17 Astronomy, Stony Brook University, Stony Brook, New York, 11794, USA

18 [6] HPCAT, Carnegie Institution of Washington, Building 434E, 9700 South Cass Avenue,

19 Argonne, Illinois 60439, USA

20 *Email: gjfinkel@princeton.edu

21

22 Abstract

23   Forsterite, Mg_2SiO_4, the magnesian endmember of the olivine system, is the

24 archetypal example of an orthosilicate structure. We have conducted synchrotron-based

25 single-crystal X-ray diffraction experiments to 90 GPa on synthetic end-member

1

26   forsterite to study its equation of state and phase transitions. Upon room-temperature

27   compression, the forsterite structure is observed to 48 GPa. By fitting a 3rd order Birch-

28   Murnaghan equation of state to our compression data, we obtain the zero-pressure

29   isothermal bulk modulus, K_{0T} = 130.0(9) GPa and its pressure derivative, K_{0T}' = 4.12(7)

30   for a fixed room pressure volume, V_0 = 290.1(1) $Å^3$, in good agreement with earlier work.

31   At 50 GPa, a phase transition to a new structure (forsterite II) occurs, followed by a

32   second transition to forsterite III at 58 GPa. Forsterite III undergoes no additional phase

33   transitions until at least 90 GPa. There is a ~4.8% volume reduction between forsterite

34   and forsterite II, and a further ~4.2% volume reduction between forsterite II and III. On

35   decompression forsterite III remains until as low as 12 GPa, but becomes amorphous at

36   ambient conditions. Using our X-ray diffraction data together with an evolutionary

37   crystal structure prediction algorithm and metadynamics simulations, we find that

38   forsterite II has triclinic space group *P1* and forsterite III has orthorhombic space group

39   *Cmc2_1*. Both high-pressure phases are metastable. Metadynamics simulations show a

40   stepwise phase transition sequence from 4-coordinated Si in forsterite to mixed

41   tetrahedral and octahedral Si (forsterite II), and then fully 6-coordinated Si (forsterite

42   III), occurring by displacement in [001](100). The forsterite III structure is a member of

43   the family of post-spinel structures adopted by compositions such as $CaFe_2O_4$ and

44    $CaTi_2O_4$.

45

46   Introduction

47   There are few minerals comparable to olivine, $(Mg,Fe)_2SiO_4$, in overall

48   importance. On Earth, olivine occurs widely in igneous and metamorphic rocks (Deer et

49   al., 1982) and is the dominant mineral phase of Earth's upper mantle (Ringwood, 1991).

50   It is also found in meteorites (Mason, 1963), comets (Crovisier et al., 1997; Zolensky et

51   al., 2006), pre-solar grains (Nguyen and Zinner, 2004), other planets (Mustard et al.,

52   2005), and in accretion disks around young stars (van Boekel et al., 2004). In the Earth's

53   upper mantle, phase transitions in Mg-rich olivine and its polymorphs are believed to be

54   responsible for the major seismic discontinuities at 410-, 520-, and 660-km depth

55   (Ringwood, 1991).. Olivine's creep behavior exerts a major control on mantle rheology

56   and affects the interpretation of seismic anisotropy (Karato and Wu, 1993). While

57   olivine transforms to wadsleyite at a depth near 410 km (~14 GPa) at normal mantle

58   temperatures, it may persist metastably in cold subducting lithosphere below 410 km

59   depth and play a role in deep earthquake generation (Kirby et al., 1996; Kawakatsu and

60   Yoshioka, 2011). There has also been interest in the behavior of amorphous and liquid

61   Mg_2SiO_4 over a wide range of pressures as a model system for understanding partial

62   melting of the mantle, production of basalts and komatiites, and the behavior of magma

63   oceans (Durben et al., 1993; de Koker et al., 2008; Adjaoud et al., 2011).

64   The structure of olivine (*Pbnm*, Z=4) can be described as an expanded and

65   distorted hexagonally close-packed (hcp) array of oxygen anions stacked along the *a*

66   direction (Bragg and Brown, 1926; Smyth et al., 2000). Si cations are located in

67   tetrahedral sites, and Mg is in two distinct octahedral sites, one of which (M2) is larger

68   and more distorted than the other (M1). Si-O tetrahedra are isolated and share corners

69   with Mg-O octahedra, while the Mg-O octahedra share both corners and edges. There are

70   three distinct oxygen sites: O1 and O2 are located on a mirror plane, while O3 is in a

71   general position. Each oxygen anion is bonded to three octahedral cations and one

72   tetrahedral cation. The addition of Fe slightly expands the unit cell and increases its

73   distortion (Birle et al., 1968).

74   There is considerable controversy over the 300 K compression behavior in the

75   olivine system. Above ~14 GPa, forsterite becomes metastable under 300-K

3

76 compression. Previous studies report evidence for amorphization (Guyot and Reynard,

77 1992; Durben et al., 1993; Andrault et al., 1995), a change in compression mechanism

78 (Andrault et al., 1995; Rouquette et al., 2008), and a spin transition (Rouquette et al.,

79 2008) with strong Fe-Mg compositional effects (Andrault et al., 1995) at high pressures.

80 Whereas non-hydrostatic powder X-ray diffraction has been collected on forsterite up to

81 70 GPa (Andrault et al., 1995), single-crystal diffraction data have been reported only to

82 17 GPa (Downs et al., 1996). Due to the limitations of powder X-ray diffraction and

83 spectroscopic studies, previous work has not been able to determine convincingly

84 whether forsterite goes through a phase transition, amorphization, or a change in

85 compression mechanism.

86 Single-crystal studies using laboratory-based X-ray sources have yielded

87 important information on the equation of state and crystal structure variation of mantle

88 minerals (Hazen and Finger, 1982; Miletich et al., 2000). However, experiments with lab-

89 based X-ray sources are generally limited to a maximum pressure of ~15 GPa. Recent

90 advances in high-pressure single-crystal diffraction techniques using synchrotron

91 sources (Dera et al., 2009; Dubrovinsky et al., 2010; Lavina et al., 2010; Dera et al.,

92 2011a; Dera et al., 2011b; Lavina et al., 2011; Kantor et al., 2012; Merlini et al., 2012)

93 allow for the use of smaller and thinner crystals ($\sim$ 5-10 μm), which can be compressed

94 to pressures approaching one megabar while retaining a quasi-hydrostatic stress

95 environment. Single-crystal X-ray diffraction is particularly useful for investigating low-

96 symmetry materials such as olivine. It eliminates the peak overlaps prevalent in powder

97 diffraction and yields reliable peak intensities, allowing for the extraction of precise

98 lattice constants and structural parameters. In this study, we have used single-crystal

99 diffraction in conjunction with molecular modeling to investigate the compression of

100 forsterite to 90 GPa and identify two new phase transitions to metastable structures.

101

102   Methods

103   A synthetic crystal of forsterite, Mg_2SiO_4, was used. The sample was characterized

104   at ambient conditions by X-ray diffraction, microprobe analysis, and Raman

105   spectroscopy. No impurities at detectable levels were identified. The unit cell

106   parameters at ambient pressure are a = 4.7543(5) Å, b = 10.201(2) Å, and c = 5.9819(8)

107   Å, in good agreement with literature values (Smyth and McCormick, 1995). Small

108   crystals were polished to ≤7 μm thickness and pre-screened by synchrotron X-ray

109   diffraction at beamline 13-BM-C of the GSECARS sector of the Advanced Photon Source

110   (APS), Argonne National Laboratory. Crystals with sharp, circular diffraction peaks and

111   off-axis crystal orientations were selected for further study.

112   High-pressure X-ray diffraction experiments were performed at the 16-ID-B

113   beamline of the HPCAT sector and 13-BM-D of the GSECARS sector of the APS. Pressure

114   was generated using a symmetric-type diamond anvil cell with 200 μm diameter culets.

115   The sample chamber was formed by drilling a ~110 μm hole in a rhenium gasket that

116   had been pre-indented to ~30 μm thickness. Three 10 μm x 10 μm forsterite crystals

117   were loaded into the sample chamber (Figure 1). An annealed ruby ball and a ~10 μm

118   gold foil were also included for pressure calibration (Fei et al., 2007). Pressures were

119   calculated using the gold (111) peak due to its relative insensitivity to differential stress

120   (Takemura and Dewaele, 2008). To achieve quasi-hydrostatic conditions, the cell was

121   loaded with a helium pressure-transmitting medium using the GSECARS/COMPRES gas-

122   loading system. Rare gas solids such as helium provide optimum quasi-hydrostatic

123   conditions at high pressures (Angel et al., 2007). An X-ray transparent cubic boron

124   nitride (cBN) backing plate (seat) was used on the upstream diamond, while a tungsten

125   carbide (WC) seat with a 60° opening-angle was used as the downstream seat.

5

126   Monochromatic diffraction experiments were performed at HPCAT using X-rays

127   with a wavelength of 0.3989 Å and at GSECARS with a wavelength of 0.3344 Å.

128   Diffraction patterns were collected using a Mar CCD detector that was calibrated with a

129   CeO_2 standard using the program FIT2D (Hammersley et al., 1996). The forsterite

130   crystals were compressed in ~3-6 GPa steps using a gas-membrane drive. At each

131   pressure, a wide ω scan was collected for each crystal, and at selected pressures, a

132   stepped ω scan was carried out. The ω rotation is about the vertical axis of the

133   diffractometer. Wide scans consisted of a 48° rotation of the diamond cell in ω while the

134   detector was exposed. These were used to extract d-spacings, azimuthal angles around

135   the beam center, and peak intensities. Step scans consisted of individual exposures taken

136   at 1° intervals to constrain the ω angle of maximum intensity for each peak. This provides

137   the third spatial coordinate necessary for reconstructing the crystal's reciprocal lattice,

138   which is used to index the diffraction pattern. Wide scans and step scans were taken at

139   the central detector position, as well as at lateral detector positions shifted ±70 cm in

140   order to increase spatial coverage.

141   Peak fitting was performed using the program GSE_ADA (Dera et al., 2009).

142   Polarization, Lorentz, and empirically determined diamond absorption corrections were

143   applied to the fit peaks. The reciprocal lattices for each crystal were reconstructed using

144   the software RSV (Dera et al., 2009). The unit cell and orientation matrix was found in

145   RSV for each crystal by comparing combinations of reciprocal lattice point difference

146   vectors. Twin domain orientations were identified using the program CELL_NOW

147   (Bruker AXS Inc.). Transformations to conventional unit cells were determined using

148   XPREP (Sheldrick, 2008), and lattice parameters were refined in RSV using a least-

149   squares fitting procedure. Crystal structures at selected pressures were refined in Shelx-

150   97 (Sheldrick, 2008).

6

151   Experimental unit cell parameters were used as constraints in a global structure

152   optimization using the evolutionary algorithm USPEX (Glass et al., 2006; Oganov and

153   Glass, 2006; Oganov et al., 2011; Lyakhov et al., 2013). This method searches for the

154   global minimum of the relevant thermodynamic potential and has led to the discovery of

155   new materials, including mineral phases (Oganov et al., 2006; Ma et al., 2009; Oganov et

156   al., 2009; Oganov et al., 2010). We conducted searches at fixed volume and T = 0 K, and

157   the relevant thermodynamic potential to be minimized was the internal energy. We

158   conducted several searches, both with experimental cell parameters (with 28

159   atoms/cell), and with the same cell doubled in the *c*-direction (with 56 atoms/cell). In

160   these searches, each generation consisted of 40 structures. A random symmetric

161   algorithm using all orthorhombic space groups produced the first generation and 30% of

162   each subsequent generation (Zhu et al., 2012; Lyakhov et al., 2013). Another 30% of

163   each new generation were produced by heredity, 30% by softmutation (Lyakhov et al.,

164   2010), and 10% by Mg-Si atomic permutation. All structures were relaxed within the

165   fixed unit cell. For structure relaxations and energy calculations we used the GULP code

166   (Gale, 2005) and ionic shell model with previously published parameters (Catlow, 1977;

167   Sanders et al., 1984; Lewis and Catlow, 1985). These structure searches found the

168   optimum structure in ~30 minutes on a single-core PC. The four lowest-energy

169   structures were selected and relaxed (both with fixed cell and with full relaxation) using

170   *ab initio* calculations.

171   Phase transition mechanisms for high-pressure phases were explored by

172   metadynamics in conjunction with classical molecular dynamics (MD) simulations. The

173   simulation box contained 672 ions, which corresponds to a 4x2x3 super-cell of the initial

174   forsterite structure. First, this cell was equilibrated by molecular dynamics at *P*=50 GPa

175   and *T*=1000 K in the *NPT* ensemble, i.e., at constant pressure and temperature. Particle

7

176   interactions were modeled using an advanced ionic potential (Jahn and Madden, 2007)

177   that has been shown to be accurate for a wide range of pressures and temperatures, and

178   was used successfully in previous studies of MgSiO$_3$ high-pressure phases (Jahn and

179   Martoňák, 2008; Haigis et al., 2012) and forsterite grain and phase boundary structures

180   (Gurmani et al., 2011; Adjaoud et al., 2012). A Nosé-Hoover thermostat coupled to a

181   barostat controlled temperature and pressure (Martyna et al., 1994). For the numerical

182   integration of the equations of motion, a time step of 1 femtosecond was used.

183   As the experimentally observed phase transitions do not occur spontaneously

184   during an MD simulation, metadynamics was used to force the system into a different

185   state. In the present case, an algorithm described in Martoňák et al. (2006) was used that

186   employs the components of the scaled simulation cell matrix as collective variables. The

187   scaled coordinates were defined using the Hessian matrix calculated from the initial

188   configuration that came from the MD simulation. A Gaussian height of 8.32 eV and a

189   Gaussian width of 2.88 eV$^{1/2}$ were used as metadynamics parameters. In each

190   metadynamics step, a short MD simulation of 1ps was performed to relax the atomic

191   positions and to obtain an average stress tensor for the respective configuration. In total,

192   1000 metadynamics steps were performed. This is the same approach used by Jahn and

193   Martoňák (2008) to study phase transitions in orthoenstatite.

194   Lowest-energy structures from both global structure optimization and

195   metadynamics were selected and relaxed using *ab initio* calculations in the framework of

196   density-functional theory (DFT) using the planewave code ABINIT (Gonze et al., 2009).

197   The planewave basis set was expanded to 1000 eV and optimized norm-conserving

198   pseudopotentials were used (Rappe et al., 1990). The exchange-correlation functional

199   was treated in the in the generalized gradient approximation (Perdew et al., 1996).

200   Appropriate k-point grids optimized by ABINIT were chosen to sample the Brillouin

8

201   zones of the different unit cells. For each structure, full optimization was performed at a

202   given target pressure, which includes atomic positions and unit cell parameters.

203

204   Results and Discussion

205   The measured X-ray diffraction patterns were consistent with the olivine

206   structure to 48 GPa, indicating that at 300 K forsterite can persist metastably at

207   pressures well above the ~14-GPa transition to the wadsleyite structure observed under

208   high-temperature conditions. Results from a representative structure refinement of

209   forsterite are shown in Table 1. At 50 GPa, an abrupt change in the diffraction pattern

210   was observed (Figure 2), indicating the presence of a new phase (designated as

211   forsterite II). Slight variations were observed in the transition pressure across the three

212   crystals in the cell as a result of a small pressure gradient. The crystals were preserved

213   across the transition, but the high-pressure phase was twinned, necessitating the

214   application of twin laws to index all the diffraction peaks. At 58 GPa, the diffraction

215   pattern changed again indicating the formation of a second high-pressure phase

216   (forsterite III). Unlike forsterite II, this phase is untwinned. This sequence of twinning

217   among the phases is likely controlled by symmetry changes between each structure. The

218   diffraction peaks from forsterite III show significant diffuse scattering, indicative of a

219   high density of defects in the crystal. In addition, some extra peaks are visible adjacent to

220   the main diffraction peaks that could be related to residual twin domains, but cannot be

221   indexed due to their proximity to the main diffraction peaks (Figure 2). Forsterite III was

222   observed to 90 GPa, at which point diamond failure ended the experiment. The sequence

223   of phase transitions, twinning, and diffuse scattering were reproduced in three

224   additional experimental runs, each involving 2 or more crystals. In one run, forsterite III

9

225   remained crystalline on decompression until at least 12 GPa, but became amorphous at

226   ambient pressure.

227   Lattice parameter and volume compression data for Mg_2SiO_4 are shown in

228   Figures 3 and 4 and Table 2. The volume-pressure data to 48 GPa were fit with a 3rd

229   order Birch-Murnaghan equation of state (Figure 3). Using the measured ambient-

230   pressure unit cell volume (V_0) of 290.1(1) $Å^3$ and fixing the ambient-pressure isothermal

231   bulk modulus (K_{0T}) at 127.5 GPa, we obtain a value of 4.31(1) for the first pressure-

232   derivative of the bulk modulus (K_{0T}'). The ambient-pressure adiabatic bulk modulus of

233   forsterite has been well characterized from ultrasonic, resonance, and Brillouin

234   measurements and has a mean value of 128.8(5) GPa (Zha et al., 1996; Isaak, 2001). The

235   corresponding isothermal bulk modulus is 127.5 GPa obtained using $K_{0T} = K_{0S}/(1+\alpha\gamma_{th}T)$

236    $_{th}T)$, where α is the thermal expansivity, γ_{th} is the thermal Gruneisen parameter, and T is

237   temperature. Values for α and γ_{th} are from Anderson and Isaak (1995).

238   If both K_{0T} and K_{0T}' are allowed to vary, the resultant fit parameters are: $K_{0T} =$

239   130.0(9) GPa and $K_{0T}' = 4.12(7)$. If the Vinet equation of state (Vinet et al., 1989) is used

240   for fitting instead, the results are: $K_{0T} = 129(1)$ GPa and $K_{0T}' = 4.33(8)$. K_{0T}' values from

241   previous static compression studies (Kudoh and Takeuchi, 1985; Will et al., 1986;

242   Andrault et al., 1995; Downs et al., 1996; Zhang, 1998) range from 4.0-4.3, whereas a

243   Brillouin scattering study to 16.2 GPa (Zha et al., 1996) resulted in $K_{0T}' = 4.2(2)$ (Table

244   3). Values for the pressure-derivative of the bulk modulus, as reported in previous

245   theoretical studies of forsterite using density functional theory, range from 4.0-4.3 (da

246   Silva et al., 1997; Li et al., 2007; Ottonello et al., 2009). Within uncertainty, K_{0T}' values

247   from all three of these different techniques (computation, X-ray diffraction, Brillouin

248   scattering) are in good agreement with each other and with our results.

249 For the individual lattice parameters, we find that the most to least compressible

250 axes are, in order, $b>c>a$, in agreement with previous studies on forsterite. Axial

251 compression data were fit to a modified third-order Birch-Murnaghan equation (Xia et

252 al., 1998). The compression behavior of the lattice parameters is similar to that reported

253 in previous single-crystal studies (Downs et al., 1996; Zha et al., 1998), and varies

254 smoothly up to the phase transition pressure (Figure 4). Linear compressibilities were

255 calculated from fits to the axial compressibility data and are in good agreement with

256 values constrained independently from measurements of elastic constants (Isaak et al.,

257 1989; Zha et al., 1996) (Figure 5).

258 In comparison with a previous powder X-ray diffraction study by Andrault et al.

259 (1995), our results show significant differences in the a and b parameters at high

260 pressures (Figure 4). At 40-50 GPa, Andrault et al. noted a change in the slope of all three

261 of the lattice parameters and proposed a change in the compression mechanism of

262 forsterite. In addition, they note the appearance of a small number of new diffraction

263 peaks at ~35 GPa, and conclude that these peaks are the result of the partial

264 transformation of olivine to a spinel-like structure. They hypothesize that this transition

265 is not completed due to slow kinetics compared with pressure-induced amorphization,

266 which they propose is the main process of structural reorganization in forsterite at high

267 pressure and 300 K.

268 In a non-hydrostatic Raman spectroscopic study to 50 GPa (Durben et al., 1993)

269 two new Raman bands were observed above 30 GPa. These were interpreted as being

270 related to a defective olivine structure in which adjacent SiO_4 polyhedra polymerized

271 upon compression as a predecessor to pressure-induced amorphization. Additional non-

272 hydrostatic powder X-ray and Mossbauer data on an Fe-bearing olivine (Rouquette et al.,

11

273   2008) are also consistent with the lattice parameter and unit cell volume trends seen by

274   Andrault et al.

275   In this work we observe no changes in the forsterite diffraction pattern or

276   compression trends to 48 GPa and no evidence for amorphization. These differences

277   may reflect the role of non-hydrostatic stresses in the previous experiments. However,

278   interpretation of the earlier powder diffraction experiments is hindered by their poor

279   signal-to-noise ratio and low angular resolution. The proposed change in compression

280   mechanism from previous work may instead be transformation to the forsterite II phase

281   near 50 GPa. It is also notable that shock compression data for Mg-rich olivine show a

282   mixed-phase region indicating a high-pressure phase transition beginning from about 50

283   GPa (Brown et al., 1987).

284   The diffraction data for forsterite II show that it is a triclinic phase with unit cell

285   lengths similar to those of forsterite. At 52 GPa, the lattice parameters are a = 4.683(2) Å,

286   b = 9.21(3) Å, c = 5.317(6) Å, α = 93.0(2)°, β = 106.94(5)°, and γ = 97.8(1)°. Forsterite II

287   was observed in diffraction patterns between 50.1 GPa, and 55.2 GPa; however, a step

288   scan was only carried out at 52.4 GPa and so the unit cell has been determined only at

289   this pressure (Figure 3). The volume reduction associated with the transition is ~4.8%.

290   The unit cell of forsterite III was constrained from diffraction data between 58.2

291   and 89.9 GPa. It is a base-centered orthorhombic cell, characterized by an a-axis that is

292   approximately one third that of b and c (Table 2). At 58.2 GPa, the lattice parameters are

293   a = 2.640(2) Å, b = 8.596(8) Å, and c = 9.04(4) Å. The c-parameter has larger uncertainty

294   as a result of the diffuse scattering (and therefore disorder) observed in that direction.

295   There is a clear relationship between the initial low-pressure forsterite unit cell and the

296   unit cell of forsterite III, as the a-, b-, and c-parameters of forsterite III are, respectively,

12

297   half the *c*-parameter, double the *a*-parameter, and the same as the *b*-parameter of

298   forsterite.

299   Analysis of systematic absences places the new structure in the orthorhombic

300   Patterson group *Cmmm*. Structure searches using USPEX and the experimental cell

301   parameters at 58.2 GPa established the structure and its space group, $Cmc2_1$, which is an

302   acentric subgroup of the *Cmcm* space group. At the experimental cell parameters, the

303   simulations show that the model structure has a hydrostatic stress tensor consistent

304   with the experimental pressure.

305   Metadynamics simulations revealed a step-wise phase transition sequence

306   consistent with our experimental findings. The transitions occur by shear deformation of

307   forsterite in [001](100) with displacement vectors of approximately 1/4 **c** + 1/12 **b.** This

308   results in a change in stacking sequence of the oxygen structure from hexagonal to

309   cubic-like, and changes the Si coordination from 4 to 6. After ~600 metadynamics steps,

310   half of the Si ions are in 6-fold coordination and the structure is characterized by

311   alternating layers of octahedral and tetrahedral Si. The volume is reduced by ~5%.

312   Between metadynamics steps 600 and 700, the intermediate structure is further

313   compressed by similar shear deformations, which results in a subsequent increase in the

314   number of octahedral Si atoms, although 5-fold coordinated Si are also observed. The

315   final structure, which is similar, but not identical, to the structure found using USPEX,

316   has a volume that is about 10% smaller than the original forsterite and essentially all Si

317   in an octahedral environment. These volume reductions are consistent with those

318   observed experimentally between forsterite, forsterite II, and forsterite III. The

319   remaining disorder on the Si sites may be due to the large shear stresses involved in

320   metadynamics and incomplete annealing. In addition, there are some stacking faults, but

321   those could be equally present in the experiment, as indicated by the observed diffuse

13

322   scattering in the diffraction patterns of the high-pressure forsterite structures. For the

323   comparison between metadynamics and experiment, it should be kept in mind that

324   shear deformation in real samples should involve dislocations that are not modeled

325   here. The small system size only allows for homogeneous shear, which requires

326   unrealistic shear stresses. However, with metadynamics easy shear planes are readily

327   identified, which makes the proposed mechanism to the post-spinel phase a plausible

328   one.

329   A candidate structure for forsterite II was also extracted from the metadynamics

330   simulations. The repeat unit of the structure obtained after ~600 metadynamics steps

331   contained 112 atoms and Si in both tetrahedral and octahedral coordination. Closer

332   inspection suggested the presence of (100) stacking faults. After their removal, a *P1*

333   triclinic unit cell with 28 atoms and lattice parameters similar to the experimental ones

334   was extracted (Table 4 and Figure 6). Structure refinements from the experimental data

335   were not possible due to extensive twinning of the crystal as well as the low peak-to-

336   parameter ratio in the refinement. The DFT refined lattice parameters at 52.4 GPa are *a*

337   = 4.695 Å, *b* = 9.201 Å, *c* = 5.311 Å, α = 93.100°, β = 107.264°, and γ = 98.133°, which are

338   consistent with the experimental values reported above. The atomic positions are given

339   in Table 4. This structure consists of a framework of edge-sharing Mg polyhedra, one-

340   quarter of which are 7-coordinated in a pentagonal bipyramid configuration, and three-

341   quarters of which are octahedrally coordinated. Half of the Si is octahedrally

342   coordinated, and half is tetrahedrally coordinated. Each of two edge-sharing Si

343   octahedra shares a corner with a Si tetrahedron to form isolated four-membered Si

344   polyhedral chains (tetrahedron-octahedron-octahedron-tetrahedron) that are kinked

345   between the tetrahedra and octahedra. When viewed along [001], the structure consists

14

346   of layers of Mg and Si octahedra alternating with layers of Si tetrahedra and Mg

347   pentagonal bipyramids (Figure 6).

348   AB_2O_4 compounds commonly adopt the spinel structure. High-pressure

349   transformations in oxide spinels can involve various disproportionation pathways

350   (perovskite + oxide, rutile + oxide, ilmenite + oxide), formation of a distorted spinel

351   (Greenberg et al., 2011), or transformation to one of several post-spinel structures such

352   as calcium ferrite and related structures ($CaFe_2O_4$, $CaTi_2O_4$, $CaMn_2O_4$) (Reid and

353   Ringwood, 1969; Andrault and Bolfan-Casanova, 2001; Chen et al., 2003; Dubrovinsky et

354   al., 2003; Yamanaka et al., 2008). The $CaFe_2O_4$-type phase is believed to be an important

355   host for aluminum in subducted basaltic oceanic crust (Ono et al., 2002). On the basis of

356   lattice parameter ratios alone, a post-spinel structure could be identified as a possible

357   candidate for forsterite III, and this was confirmed by the structure solution calculations.

358   Thus, under room-temperature compression, forsterite transforms via a triclinic

359   intermediate structure (forsterite II) over a narrow pressure range to a post-spinel

360   structure, in sharp contrast to its high-temperature transformation sequence from

361   olivine to spinelloid to spinel to perovskite and oxide. However, it should be noted that

362   DFT calculations show forsterite II and III to be energetically metastable when

363   compared with their high-temperature counterparts.

364   Post-spinel phases are characterized by chains of edge- and corner-sharing

365   octahedra with channels that run parallel to the c-axis. Changes in octahedral linkage

366   and site distortion differentiate the individual members in this family. Depending on the

367   cation and anion sizes, the ions that reside in the channels can have different

368   coordination. The most frequently observed post-spinel structures are the $CaMn_2O_4$-,

369    $CaFe_2O_4$-, and $CaTi_2O_4$-type structures (Yamanaka et al., 2008), but for forsterite III, the

370   most energetically (meta)stable structure is a non-centrosymmetric version of the *Cmcm*

15

371    $CaTi_2O_4$-type structure, in which half of the Mg ions (Mg2 site) reside in the face-sharing

372   trigonal prismatic site (the *c*-axis-oriented channels), while the other half of the Mg ions

373   (Mg1 site) share the octahedral Ti site with the Si ions (Figure 7). This arrangement is

374   analogous to an inverse spinel, since the larger cation, Mg^{2+}, occupies both the larger

375   trigonal prismatic site and the smaller octahedral site.

376   Since we only have a limited number of observed unique diffraction peaks (24 at

377   58.2 GPa) compared with the number of refinable parameters in the proposed forsterite

378   III structure (1 free variable, 14 positional parameters, and 7 isotropic thermal

379   displacement parameters), we refined the structure by alternating refinements between

380   the cations and anions until the refinement was nearly complete. At that point we fixed

381   the isotropic thermal displacement parameters, and refined all the atomic position

382   coordinates together. The refined structure is similar to the structure proposed by

383   theory, but with more distorted coordination polyhedra (see Table 5 for atomic

384   coordinates from experiment and theory and Figure 7 for a visual comparison). The

385   most significant difference is that for the M2 site, the Mg ions move far enough away

386   from the centers of the trigonal prisms that they become 7-coordinated in a capped

387   trigonal prism configuration. However, this refinement should be considered

388   preliminary due to the low peak-to-parameter ratio.

389   While the uncertainty in the unit cell parameters is relatively large for the high-

390   pressure phase, there is clearly a substantial volume decrease associated with the phase

391   transition sequence. The volume of forsterite III is ~9% lower than the extrapolated

392   volume of forsterite I, consistent with the metadynamics calculations. For comparison,

393   the volume difference between forsterite and the high P-T polymorphs wadsleyite and

394   ringwoodite are 7.6% and 10.4%, respectively, at ambient conditions.

16

395   In summary, our combined experimental data and theoretical calculations have

396   revealed the existence of new metastable phases of forsterite above 50 GPa under room-

397   temperature compression, in contrast with earlier reports of a change in compression

398   mechanism and amorphization. Metastable olivine polymorphs are potentially

399   important for understanding phases formed in laboratory shock experiments as well as

400   those found naturally in meteorites and impact sites (Van de Moortèle et al., 2007).

401   Future work will focus on the effect of iron on high-pressure behavior in this system. In

402   addition, single-crystal diffraction studies on forsterite to higher pressures as well as

403   combined high pressure-temperature conditions are needed.

404

405   Acknowledgements

17

421

422   References

423   Adjaoud, O., Marquardt, K., and Jahn, S. (2012) Atomic structures and energies of grain

424   boundaries in Mg_2SiO_4 forsterite from atomistic modeling. Physics and Chemistry

425   of Minerals, 39(9), 749-760.

426   Adjaoud, O., Steinle-Neumann, G., and Jahn, S. (2011) Transport properties of Mg_2SiO_4

427   liquid at high pressure: Physical state of a magma ocean. Earth and Planetary

428   Science Letters, 312(3), 463-470.

429   Anderson, O.L., and Isaak, D.G. (1995) Elastic constants of mantle minerals at high

430   temperature. In T.J. Ahrens, Ed. Mineral Physics & Crystallography: A Handbook

431   of Physical Constants, AGU Reference Shelf, 2, p. 64-97. AGU, Washington, D. C.

432   Andrault, D., and Bolfan-Casanova, N. (2001) High-pressure phase transformations in

433   the $MgFe_2O_4$ and Fe_2O_3–$MgSiO_3$ systems. Physics and Chemistry of Minerals,

434   28(3), 211-217.

435   Andrault, D., Bouhifd, M.A., Itié, J.P., and Richet, P. (1995) Compression and

436   amorphization of $(Mg,Fe)_2SiO_4$ olivines: An X-ray diffraction study up to 70 GPa.

437   Physics and Chemistry of Minerals, 22(2), 99-107.

438   Angel, R.J., Bujak, M., Zhao, J., Gatta, G.D., and Jacobsen, S.D. (2007) Effective hydrostatic

439   limits of pressure media for high-pressure crystallographic studies. Journal of

440   Applied Crystallography, 40(1), 26-32.

441   Birle, J.D., Gibbs, G.V., Moore, P.B., and Smith, J.V. (1968) Crystal structures of natural

442   olivines. American Mineralogist, 53, 807-824.

18

443   Bragg, W.L., and Brown, G.B. (1926) Die struktur des olivins. Zeitschrift für

444   Kristallographie, 63, 538-556.

445   Brown, J.M., Furnish, M.D., and McQueen, R.G. (1987) Thermodynamics for $(Mg,Fe)_2SiO_4$

446   from the Hugoniot. In M. Manghnani, and Y. Syono, Eds. High Pressure Research

447   in Mineral Physics, p. 373-384. AGU, Washington, D.C.

448   Catlow, C.R.A. (1977) Point defect and electronic properties of uranium dioxide.

449   Proceedings of the Royal Society of London. A. Mathematical and Physical

450   Sciences, 353(1675), 533-561.

451   Chen, M., Shu, J., Mao, H.K., Xie, X., and Hemley, R.J. (2003) Natural occurrence and

452   synthesis of two new postspinel polymorphs of chromite. Proceedings of the

453   National Academy of Sciences, 100(25), 14651-14654.

454   Crovisier, J., Leech, K., Bockelée-Morvan, D., Brooke, T.Y., Hanner, M.S., Altieri, B., Keller,

455   H.U., and Lellouch, E. (1997) The spectrum of comet Hale-Bopp (C/1995 O1)

456   observed with the Infrared Space Observatory at 2.9 astronomical units from the

457   Sun. Science, 275(5308), 1904-1907.

458   da Silva, C., Stixrude, L., and Wentzcovitch, R.M. (1997) Elastic constants and anisotropy

459   of forsterite at high pressure. Geophysical Research Letters, 24(15), 1963-1966.

460   de Koker, N.P., Stixrude, L., and Karki, B.B. (2008) Thermodynamics, structure, dynamics,

461   and freezing of Mg_2SiO_4 liquid at high pressure. Geochimica et Cosmochimica

462   Acta, 72(5), 1427-1441.

463   Deer, W.A., Howie, R.A., and Zussman, J. (1982) Orthosilicates. Longman, London.

464   Dera, P., Lavina, B., Borkowski, L.A., Prakapenka, V.B., Sutton, S.R., Rivers, M.L., Downs,

465   R.T., Boctor, N.Z., and Prewitt, C.T. (2009) Structure and behavior of the

466   barringerite Ni end-member, Ni_2P, at deep Earth conditions and implications for

19

467   natural Fe-Ni phosphides in planetary cores. Journal of Geophysical Research,

468   114(B3), B03201.

469 Dera, P., Lazarz, J.D., and Lavina, B. (2011a) Pressure-induced development of bonding in

470   NiAs type compounds and polymorphism of NiP. Journal of Solid State Chemistry,

471   184(8), 1997-2003.

472 Dera, P., Lazarz, J.D., Prakapenka, V.B., Barkley, M., and Downs, R.T. (2011b) New insights

473   into the high-pressure polymorphism of SiO_2 cristobalite. Physics and Chemistry

474   of Minerals, 38(7), 1-13.

475 Downs, R.T., Zha, C.S., Duffy, T.S., and Finger, L.W. (1996) The equation of state of

476   forsterite to 17.2 GPa and effects of pressure media. American Mineralogist, 81(1-

477   2), 51-55.

478 Dubrovinsky, L., Boffa-Ballaran, T., Glazyrin, K., Kurnosov, A., Frost, D., Merlini, M.,

479   Hanfland, M., Prakapenka, V.B., Schouwink, P., and Pippinger, T. (2010) Single-

480   crystal X-ray diffraction at megabar pressures and temperatures of thousands of

481   degrees. High Pressure Research, 30(4), 620-633.

482 Dubrovinsky, L.S., Dubrovinskaia, N.A., McCammon, C., Rozenberg, G.K., Ahuja, R., Osorio-

483   Guillen, J.M., Dmitriev, V., Weber, H.P., Bihan, T.L., and Johansson, B. (2003) The

484   structure of the metallic high-pressure Fe_3O_4 polymorph: experimental and

485   theoretical study. Journal of Physics: Condensed Matter, 15(45), 7697-7706.

486 Durben, D.J., McMillan, P.F., and Wolf, G.H. (1993) Raman study of the high-pressure

487   behavior of forsterite (Mg_2SiO_4) crystal and glass. American Mineralogist, 78(11-

488   12), 1143-1148.

489 Fei, Y., Ricolleau, A., Frank, M., Mibe, K., Shen, G., and Prakapenka, V. (2007) Toward an

490   internally consistent pressure scale. Proceedings of the National Academy of

491   Sciences, 104(22), 9182-9186.

20

492   Gale, J.D. (2005) GULP: capabilities and prospects. Zeitschrift für Kristallographie, 220(5-

493   6), 552-554.

494   Glass, C.W., Oganov, A.R., and Hansen, N. (2006) USPEX — evolutionary crystal structure

495   prediction. Computer Physics Communications, 175(11), 713-720.

496   Gonze, X., Amadon, B., Anglade, P.M., Beuken, J.M., Bottin, F., Boulanger, P., Bruneval, F.,

497   Caliste, D., Caracas, R., and Cote, M. (2009) ABINIT: First-principles approach to

498   material and nanosystem properties. Computer Physics Communications,

499   180(12), 2582-2615.

500   Greenberg, E., Dubrovinsky, L.S., McCammon, C., Rouquette, J., Kantor, I., Prakapenka, V.,

501   Rozenberg, G.K., and Pasternak, M.P. (2011) Pressure-induced structural phase

502   transition of the iron end-member of ringwoodite (γ-Fe_2SiO_4) investigated by X-

503   ray diffraction and Mössbauer spectroscopy. American Mineralogist, 96(5-6),

504   833-840.

505   Gurmani, S.F., Jahn, S., Brasse, H., and Schilling, F.R. (2011) Atomic scale view on partially

506   molten rocks: Molecular dynamics simulations of melt-wetted olivine grain

507   boundaries. Journal of Geophysical Research, 116(B12), B12209.

508   Guyot, F., and Reynard, B. (1992) Pressure-induced structural modifications and

509   amorphization in olivine compounds. Chemical Geology, 96(3-4), 411-420.

510   Haigis, V., Salanne, M., and Jahn, S. (2012) Thermal conductivity of MgO, $MgSiO_3$

511   perovskite and post-perovskite in the earth's deep mantle. Earth and Planetary

512   Science Letters, 355-356, 102-108.

513   Hammersley, A.P., Svensson, S.O., Hanfland, M., Fitch, A.N., and Hausermann, D. (1996)

514   Two-dimensional detector software: From real detector to idealised image or

515   two-theta scan. High Pressure Research, 14(4-6), 235-248.

21

516   Hazen, R.M., and Finger, L.W. (1982) Comparative crystal chemistry: Temperature,

517   pressure, composition, and the variation of crystal structure. 250 p. Wiley.

518   Isaak, D.G. (2001) Elastic properties of minerals and planetary objects. In M. Levy, J.D.

519   Bass, and R. Stern, Eds. Handbook of Elastic Properties of Solids, Liquids, and

520   Gases: Volume III: Elastic Properties of Solids: Biological and Organic Material,

521   Earth and Marine Sciences, p. 325-376. Academic Press, San Diego.

522   Isaak, D.G., Anderson, O.L., and Goto, T. (1989) Elasticity of single-crystal forsterite

523   measured to 1700 K. Journal of Geophysical Research, 94(B5), 5895-5906.

524   Jahn, S., and Madden, P.A. (2007) Modeling Earth materials from crustal to lower mantle

525   conditions: A transferable set of interaction potentials for the CMAS system.

526   Physics of the Earth and Planetary Interiors, 162(1), 129-139.

527   Jahn, S., and Martoňák, R. (2008) Plastic deformation of orthoenstatite and the ortho-to

528   high-pressure clinoenstatite transition: A metadynamics simulation study.

529   Physics and Chemistry of Minerals, 35(1), 17-23.

530   Kantor, A., Kantor, I., Merlini, M., Glazyrin, K., Prescher, C., Hanfland, M., and

531   Dubrovinsky, L. (2012) High-pressure structural studies of eskolaite by means of

532   single-crystal X-ray diffraction. American Mineralogist, 97(10), 1764-1770.

533   Karato, S., and Wu, P. (1993) Rheology of the upper mantle: A synthesis. Science,

534   260(5109), 771-778.

535   Kawakatsu, H., and Yoshioka, S. (2011) Metastable olivine wedge and deep dry cold slab

536   beneath southwest Japan. Earth and Planetary Science Letters, 303(1-2), 1-10.

537   Kirby, S.H., Stein, S., Okal, E.A., and Rubie, D.C. (1996) Metastable mantle phase

538   transformations and deep earthquakes in subducting oceanic lithosphere.

539   Reviews of Geophysics, 34(2), 261-306.

22

540   Kudoh, Y., and Takeuchi, Y. (1985) The crystal structure of forsterite Mg_2SiO_4 under high

541   pressure up to 149 kb. Zeitschrift für Kristallographie, 171(3-4), 291-302.

542   Lavina, B., Dera, P., Kim, E., Meng, Y., Downs, R.T., Weck, P.F., Sutton, S.R., and Zhao, Y.

543   (2011) Discovery of the recoverable high-pressure iron oxide Fe_4O_5. Proceedings

544   of the National Academy of Sciences, 108(42), 17281-17285.

545   Lavina, B., Dera, P.K., Downs, R.T., Yang, W., Sinogeikin, S.V., Meng, Y., Shen, G., and

546   Schiferl, D. (2010) Structure of siderite $FeCO_3$ to 56 GPa and hysteresis of its spin-

547   pairing transition. Physical Review B, 82(6), 064110.

548   Lewis, G.V., and Catlow, C.R.A. (1985) Potential models for ionic oxides. Journal of

549   Physics C: Solid State Physics, 18(6), 1149-1161.

550   Li, L., Wentzcovitch, R.M., Weidner, D.J., and Da Silva, C.R.S. (2007) Vibrational and

551   thermodynamic properties of forsterite at mantle conditions. Journal of

552   Geophysical Research, 112(B5), B05206.

553   Lyakhov, A.O., Oganov, A.R., Stokes, H.T., and Zhu, Q. (2013) New developments in

554   evolutionary structure prediction algorithm USPEX. Computer Physics

555   Communications, 184(4), 1172-1182.

556   Lyakhov, A.O., Oganov, A.R., and Valle, M. (2010) How to predict very large and complex

557   crystal structures. Computer Physics Communications, 181(9), 1623-1632.

558   Ma, Y., Eremets, M., Oganov, A.R., Xie, Y., Trojan, I., Medvedev, S., Lyakhov, A.O., Valle, M.,

559   and Prakapenka, V. (2009) Transparent dense sodium. Nature, 458(7235), 182-

560   185.

561   Martoňák, R., Donadio, D., Oganov, A.R., and Parrinello, M. (2006) Crystal structure

562   transformations in SiO_2 from classical and ab initio metadynamics. Nature

563   Materials, 5(8), 623-626.

23

564   Martyna, G.J., Tobias, D.J., and Klein, M.L. (1994) Constant pressure molecular dynamics

565   algorithms. The Journal of Chemical Physics, 101(5), 4177-4189.

566   Mason, B. (1963) Olivine composition in chondrites. Geochimica et Cosmochimica Acta,

567   27(10), 1011-1023.

568   Merlini, M., Crichton, W.A., Hanfland, M., Gemmi, M., Müller, H., Kupenko, I., and

569   Dubrovinsky, L. (2012) Structures of dolomite at ultrahigh pressure and their

570   influence on the deep carbon cycle. Proceedings of the National Academy of

571   Sciences, 109(34), 13509-13514.

572   Miletich, R., Allan, D.R., and Kuhs, W.F. (2000) High-pressure single-crystal techniques.

573   Reviews in Mineralogy and Geochemistry, 41(1), 445-519.

574   Mustard, J.F., Poulet, F., Gendrin, A., Bibring, J.P., Langevin, Y., Gondet, B., Mangold, N.,

575   Bellucci, G., and Altieri, F. (2005) Olivine and pyroxene diversity in the crust of

576   Mars. Science, 307(5715), 1594-1597.

577   Nguyen, A.N., and Zinner, E. (2004) Discovery of ancient silicate stardust in a meteorite.

578   Science, 303(5663), 1496-1499.

579   Oganov, A.R., Chen, J., Gatti, C., Ma, Y., Glass, C.W., Liu, Z., Yu, T., Kurakevych, O.O., and

580   Solozhenko, V.L. (2009) Ionic high-pressure form of elemental boron. Nature,

581   457(7231), 863-867.

582   Oganov, A.R., and Glass, C.W. (2006) Crystal structure prediction using ab initio

583   evolutionary techniques: Principles and applications. The Journal of Chemical

584   Physics, 124(24), 244704.

585   Oganov, A.R., Glass, C.W., and Ono, S. (2006) High-pressure phases of $CaCO_3$: Crystal

586   structure prediction and experiment. Earth and Planetary Science Letters, 241(1),

587   95-103.

24

588   Oganov, A.R., Lyakhov, A.O., and Valle, M. (2011) How evolutionary crystal structure

589   prediction works and why. Accounts of Chemical Research, 44(3), 227-237.

590   Oganov, A.R., Ma, Y., Lyakhov, A.O., Valle, M., and Gatti, C. (2010) Evolutionary crystal

591   structure prediction as a method for the discovery of minerals and materials.

592   Reviews in Mineralogy and Geochemistry, 71(1), 271-298.

593   Ono, S., Hirose, K., Kikegawa, T., and Saito, Y. (2002) The compressibility of a natural

594   composition calcium ferrite-type aluminous phase to 70 GPa. Physics of the Earth

595   and Planetary Interiors, 131(3), 311-318.

596   Ottonello, G., Civalleri, B., Ganguly, J., Vetuschi Zuccolini, M., and Noel, Y. (2009)

597   Thermophysical properties of the α-β-γ polymorphs of Mg_2SiO_4: A computational

598   study. Physics and Chemistry of Minerals, 36(2), 87-106.

599   Perdew, J.P., Burke, K., and Ernzerhof, M. (1996) Generalized gradient approximation

600   made simple. Physical Review Letters, 77(18), 3865-3868.

601   Rappe, A.M., Rabe, K.M., Kaxiras, E., and Joannopoulos, J.D. (1990) Optimized

602   pseudopotentials. Physical Review B, 41(2), 1227-1230.

603   Reid, A.F., and Ringwood, A.E. (1969) Newly observed high pressure transformations in

604   Mn_3O_4, $CaAl_2O_4$, and $ZrSiO_4$. Earth and Planetary Science Letters, 6, 205-208.

605   Ringwood, A.E. (1991) Phase transformations and their bearing on the constitution and

606   dynamics of the mantle. Geochimica et Cosmochimica Acta, 55(8), 2083-2110.

607   Rouquette, J., Kantor, I., McCammon, C.A., Dmitriev, V., and Dubrovinsky, L.S. (2008)

608   High-pressure studies of $(Mg_{0.9}Fe_{0.1})_2SiO_4$ olivine using Raman spectroscopy, X-

609   ray diffraction, and Mössbauer spectroscopy. Inorganic Chemistry, 47(7), 2668-

610   2673.

611   Sanders, M.J., Leslie, M., and Catlow, C.R.A. (1984) Interatomic potentials for SiO_2. Journal

612   of the Chemical Society, Chemical Communications(19), 1271-1273.

613   Sheldrick, G.M. (2008) A short history of SHELX. Acta Crystallographica Section A:

614   Foundations of Crystallography, 64(1), 112-122.

615   Smyth, J.R., Jacobsen, S.D., and Hazen, R.M. (2000) Comparative crystal chemistry of

616   orthosilicate minerals. Reviews in Mineralogy and Geochemistry, 41(1), 187-209.

617   Smyth, J.R., and McCormick, T.C. (1995) Crystallographic data for minerals. In T.J.

618   Ahrens, Ed. Mineral Physics and Crystallography: A Handbook of Physical

619   Constants, 2, p. 1-17. AGU, Washington, D. C.

620   Takemura, K., and Dewaele, A. (2008) Isothermal equation of state for gold with a He-

621   pressure medium. Physical Review B, 78(10), 104119.

622   van Boekel, R., Min, M., Leinert, C., Waters, L.B.F.M., Richichi, A., Chesneau, O., Dominik,

623   C., Jaffe, W., Dutrey, A., Graser, U., Henning, T., Jong, J.d., hler, R., Koter, A.d., Lopez,

624   B., Malbet, F., Morel, S., Paresce, F., Perrin, G., Preibisch, T., Przygodda, F., Sch, ller,

625   M., and Wittkowski, M. (2004) The building blocks of planets within the

626   'terrestrial' region of protoplanetary disks. Nature, 432(7016), 479-482.

627   Van de Moortèle, B., Reynard, B., McMillan, P.F., Wilson, M., Beck, P., Gillet, P., and Jahn, S.

628   (2007) Shock-induced transformation of olivine to a new metastable

629         $(Mg,Fe)_2SiO_4$ polymorph in Martian meteorites. Earth and Planetary Science

630   Letters, 261(3-4), 469-475.

631   Vinet, P., Rose, J.H., Ferrante, J., and Smith, J.R. (1989) Universal features of the equation

632   of state of solids. Journal of Physics: Condensed Matter, 1(11), 1941-1963.

633   Will, G., Hoffbauer, W., Hinze, E., and Lauterjung, J. (1986) The compressibility of

634   forsterite up to 300 kbar measured with synchrotron radiation. Physica B+C, 139-

635   140, 193-197.

26

636   Xia, X., Weidner, D.J., and Zhao, H. (1998) Equation of state of brucite; single-crystal

637   Brillouin spectroscopy study and polycrystalline pressure-volume-temperature

638   measurement. American Mineralogist, 83(1-2), 68-74.

639   Yamanaka, T., Uchida, A., and Nakamoto, Y. (2008) Structural transition of post-spinel

640   phases $CaMn_2O_4$, $CaFe_2O_4$, and $CaTi_2O_4$ under high pressures up to 80 GPa.

641   American Mineralogist, 93(11-12), 1874-1881.

642   Zha, C., Duffy, T.S., Downs, R.T., Mao, H., and Hemley, R.J. (1998) Brillouin scattering and

643   X-ray diffraction of San Carlos olivine: direct pressure determination to 32 GPa.

644   Earth and Planetary Science Letters, 159(1-2), 25-33.

645   Zha, C.S., Duffy, T.S., Downs, R.T., Mao, H.K., and Hemley, R.J. (1996) Sound velocity and

646   elasticity of single-crystal forsterite to 16 GPa. Journal of Geophysical Research,

647   101(B8), 17535-17545.

648   Zhang, L. (1998) Single crystal hydrostatic compression of $(Mg,Mn,Fe,Co)_2SiO_4$ olivines.

649   Physics and Chemistry of Minerals, 25(4), 308-312.

650   Zhu, Q., Oganov, A.R., Glass, C.W., and Stokes, H.T. (2012) Constrained evolutionary

651   algorithm for structure prediction of molecular crystals: Methodology and

652   applications. Acta Crystallographica Section B: Structural Science, 68(3), 215-226.

653   Zolensky, M.E., Zega, T.J., Yano, H., Wirick, S., Westphal, A.J., Weisberg, M.K., Weber, I.,

654   Warren, J.L., Velbel, M.A., and Tsuchiyama, A. (2006) Mineralogy and petrology of

655   comet 81P/Wild 2 nucleus samples. Science, 314(5806), 1735-1739.

656
657
658
659
660
661
662
663
664
665

27

666   Figure Captions

667

668   Figure 1. Sample configuration showing three forsterite crystals, a ruby ball, and a gold

669   foil contained in a helium pressure-transmitting medium in a diamond anvil cell.

670

671   Figure 2. (a) Diffraction pattern at 48 GPa. Boxes are shown around forsterite diffraction

672   peaks that were used in the analysis. (b) Expanded image of forsterite diffraction peaks

673   in (a). (c) Diffraction pattern at 52 GPa. Indexed peaks for forsterite II are shown from

674   two different twin domains. (d) Diffraction pattern of forsterite III at 58 GPa. The arrows

675   show peaks that may be due to residual domains of forsterite II. (e) Expanded image of

676   forsterite III diffraction peaks from (d). Diffuse scattering results in distorted shapes for

677   some peaks.

678

679   Figure 3. Unit cell volume of forsterite from this study (filled symbols) compared to

680   previous powder diffraction experiments (open symbols). The shaded region shows the

681   range over which we observe forsterite II. Where not shown, error bars are smaller than

682   the symbol size.

683

684   Figure 4. Relative axial lengths of forsterite compared with selected previous studies.

685   Circles, diamonds, and squares are lattice parameters a, b, and c, respectively. Dashed

686   lines show the fits to the axial compression data.

687

688   Figure 5. Linear compressibilities along the unit cell axes for forsterite (solid lines)

689   compared with measured values from single-crystal elastic constants (open symbols).

690

28

691   Figure 6. a) A model of the forsterite II structure derived from metadynamics and

692   optimized using DFT calculations. Gray polyhedra represent Mg sites and blue polyhedra

693   Si sites. Oxygen ions are red. Si ions are located in both octahedral and tetrahedral sites,

694   and Mg ions are located in both octahedral and pentagonal bipyramidal sites. b) The Mg

695   pentagonal bipyramids in forsterite II. c) The Si tetrahedral and octahedral chains in

696   forsterite II.

697

698   Figure 7. a) A model of the forsterite III structure optimized using DFT. Gray polyhedra

699   represent Mg sites and blue polyhedra Si sites. Oxygen atoms are red. Si atoms are

700   located in octahedral sites, and Mg atoms are located in both octahedral and face-sharing

701   trigonal prism sites. b) A model of the forsterite III structure refined against

702   experimental single-crystal diffraction intensities. Mg atoms have shifted position

703   compared with the theoretical model such that half of them are now in a 7-coordinated

704   capped trigonal prism site.

29

705
706   Tables
707
708
709   Table 1.
710
711   a) Representative single-crystal structure refinement for forsterite at 45.3 GPa.
712

Beamline	16 ID-B, HPCAT, APS, ANL
Wavelength, Å	0.39891
Pressure, GPa	45.3
Temperature, K	298
Composition	Mg_2SiO_4
Symmetry	Orthorhombic, *Pbnm* (*Pnma*)
Lattice Parameters a, b, c, Å	4.5232(5), 9.274(5), 5.5467(7)
Volume, Å^3	232.7(2)
Z	4
R_{int}	0.072
Reflection Range	$-5 \leq h \leq 5$, $-5 \leq k \leq 6$, $-7 \leq l \leq 7$
Maximum θ, °	28.8
Number Independent Reflections	124
Refinement	F^2
R	0.048
wR_2	0.109

713
714   b) Refined atomic parameters for forsterite at 45.3 GPa.
715

Atom	Wyckoff position	x/a	y/b	z/c	U_{iso}
Mg1	4a	0	0	0	0.0070(7)
Mg2	4c	0.9845(5)	0.2742(6)	0.25	0.0075(7)
Si	4c	0.4250(5)	0.0964(5)	0.25	0.0070(7)
O1	4c	0.7675(12)	0.0899(10)	0.25	0.0075(13)
O2	4c	0.2271(12)	0.4407(10)	0.25	0.0061(13)
O3	8d	0.2638(8)	0.1692(7)	0.0233(6)	0.0081(10)

716
717
718
719
720
721
722
723
724
725
726
727
728
729
730

30

731
732
733   Table 2. Mg_2SiO_4 lattice parameters and unit cell volume.
734

Forsterite

Au a (Å)	P (GPa)	a (Å)	b (Å)	c (Å)	V (Å³)
	0	4.7543(5)	10.201(2)	5.9819(8)	290.1(1)
4.0317	6.4	4.7102(5)	10.004(5)	5.898(1)	277.9(2)
4.0130	9.4	4.6881(5)	9.920(4)	5.8581(6)	272.4(2)
3.9720	16.7	4.6465(4)	9.749(4)	5.7740(6)	261.6(2)
3.9499	21.2	4.6242(5)	9.646(4)	5.7320(6)	255.7(2)
3.9343	24.6	4.6092(5)	9.579(4)	5.7016(6)	251.7(2)
3.9206	27.8	4.5956(6)	9.519(5)	5.6755(7)	248.3(2)
3.9038	32.0	4.5772(5)	9.469(4)	5.6352(6)	244.2(2)
3.8937	34.7	4.5671(4)	9.424(4)	5.6190(6)	241.8(2)
3.8809	38.2	4.5514(4)	9.363(4)	5.5924(6)	238.3(2)
3.8730	40.5	4.5441(5)	9.335(4)	5.5782(6)	236.6(2)
3.8647	43.0	4.5320(5)	9.303(5)	5.5603(7)	234.4(2)
3.8569	45.3	4.5232(5)	9.274(5)	5.5467(7)	232.7(2)
3.8484	48.0	4.5125(5)	9.236(5)	5.5337(7)	230.6(2)

Forsterite II

Au a (Å)	P (GPa)	a (Å), α (°)	b (Å), β (°)	c (Å), γ (°)	V (Å³)
3.8353	52.4	4.683(2)	9.21(3)	5.317(6)	216.4(7)
		93.0(2)	106.94(5)	97.8(1)	

Forsterite III

Au a (Å)	P (GPa)	a (Å)	b (Å)	c (Å)	V (Å³)
3.8186	58.2	2.640(2)	8.596(8)	9.04(4)	205(1)
3.8082	62.1	2.630(2)	8.566(9)	8.93(4)	201(1)
3.8013	64.7	2.623(2)	8.554(9)	8.80(4)	197(1)
3.7957	66.9	2.622(2)	8.55(1)	8.79(6)	197(2)
3.7850	71.2	2.612(2)	8.52(1)	8.76(6)	195(2)
3.7774	74.4	2.606(3)	8.49(2)	8.7(1)	193(3)
3.7679	78.5	2.597(3)	8.45(2)	8.71(9)	191(3)
3.7618	81.2	2.591(3)	8.43(2)	8.70(9)	190(3)
3.7525	85.5	2.584(3)	8.40(2)	8.67(9)	188(3)
3.7433	89.9	2.574(3)	8.37(2)	8.7(1)	187(3)

735   Numbers in parentheses represent one standard deviation uncertainty in the last digit.
736
737
738
739
740
741
742
743
744
745
746

31

747   Table 3. Comparison of equation of state data for Mg-rich olivines.

748

Reference	Composition	Pressure Medium	P_{Max} (GPa)	K_{0T} (GPa)	K_{0T}'
Single-Crystal X-ray Diffraction					
This Study	Mg_{100}	He	50	130.0(9)	4.12(7)
Zhang (1998)	Mg_{100}	4:1 meth-eth	10	127(4)	4.2(8)
Downs et al. (1996)	Mg_{100}	4:1 meth-eth, Ar, He	17	125(2)	4.0(4)
Kudoh & Takeuchi (1985)	Mg_{100}	4:1 meth-eth	15	122.6*	4.3*
Zha et al. (1998)	Mg_{90}	Ne	32	128(2)	3.8(2)
Polycrystalline X-ray Diffraction					
Andrault et al. (1995)	Mg_{100}	none	42	128(8)	4.0**
Will et al. (1986)	Mg_{100}	4:1 meth-eth	30	136(1)	4.0(1)
Brillouin Spectroscopy					
Zha et al. (1996)	Mg_{100}	4:1 meth-eth, Ar, He	16	128.8(5)	4.2(2)

749

750

751

752   *Uncertainty not provided

753   **Fixed value

754

755

756   Table 4. Atomic parameters of forsterite II at 52.4 GPa optimized using DFT (a = 4.695 Å,

757   b = 9.201 Å, c = 5.311 Å, α = 93.100°, β = 107.264°, γ = 98.133°).

758

Atom	Wyckoff position	x/a	y/b	z/c	Coordination	
Mg1	1a	0.9714	0.0966	0.6415	7	760
Mg2	1a	0.0419	0.9354	0.0567	7	761
Mg3	1a	0.0026	0.6656	0.7362	6	762
Mg4	1a	0.5065	0.5160	0.8488	6	763
Mg5	1a	0.5386	0.7905	0.1388	6	764
Mg6	1a	0.0105	0.3666	0.9614	6	765
Mg7	1a	0.4746	0.2414	0.5588	6	766
Mg8	1a	0.5065	0.5161	0.3489	6	767
Si1	1a	0.0048	0.3875	0.4564	6	768
Si2	1a	0.0083	0.6445	0.2412	6	769
Si3	1a	0.6136	0.1239	0.0951	4	770
Si4	1a	0.3995	0.9081	0.6027	4	771
O1	1a	0.2702	0.8430	0.8193		772
O2	1a	0.7865	0.6995	0.9680		773
O3	1a	0.7628	0.2287	0.3717		774
O4	1a	0.2756	0.0474	0.4928		775
O5	1a	0.7429	0.1891	0.8786		776
O6	1a	0.2266	0.3325	0.7297		777
O7	1a	0.2506	0.8032	0.3262		778
O8	1a	0.7833	0.6947	0.4029		779
O9	1a	0.7924	0.4622	0.1735		780
O10	1a	0.7372	0.9845	0.2048		781
O11	1a	0.2204	0.5698	0.5243		782
O12	1a	0.7760	0.4475	0.6450		783
O13	1a	0.2685	0.1109	0.0031		784
O14	1a	0.2370	0.5847	0.0528		785
O15	1a	0.2300	0.3374	0.2947		786
O16	1a	0.7446	0.9211	0.6950		787

759

788

789

32

790 Table 5.

791

792 a) Representative single-crystal structure refinement for forsterite III at 58.2 GPa.

793

Beamline	16 ID-B, HPCAT, APS, ANL
Wavelength, Å	0.39891
Pressure, GPa	58.2
Temperature, K	298
Composition	Mg_2SiO_4
Symmetry	Orthorhombic, $Cmc2_1$
Lattice Parameters a, b, c, Å	2.640 (2), 8.596(8), 9.04(4)
Volume, Å^3	205(1)
Z	4
R_{int}	0.060
Reflection Range	$-2 \leq h \leq 2$, $-7 \leq k \leq 9$, $-5 \leq l \leq 3$
Maximum 2θ, °	24.93
Number Independent Reflections	24
Refinement	F^2
R	0.052
wR_2	0.120

794

795 b) Refined atomic parameters for forsterite III at 58.2 GPa.

796

Atom	Wyckoff position	x/a	y/b	z/c	U_{iso}
Mg1	4a	0.5	0.373(12)	0.350(13)	0.009(8)
Mg2	4a	0.5	0.889(5)	0.622(14)	0.012(8)
Si	4a	0	0.857(16)	0.000(15)	0.018(8)
O1	4a	0.5	0.983(60)	0.46(15)	0.022(14)
O2	4a	0.5	0.231(14)	0.572(55)	0.004(12)
O3	4a	0.5	0.706(14)	0.271(44)	0.023(25)
O4	4a	0.5	0.466(16)	0.181(91)	0.011(14)

797

798 c) Atomic parameters of forsterite III at 58.2 GPa optimized using DFT (a = 2.591 Å, b =

799 8.726 Å, c = 8.794 Å).

800

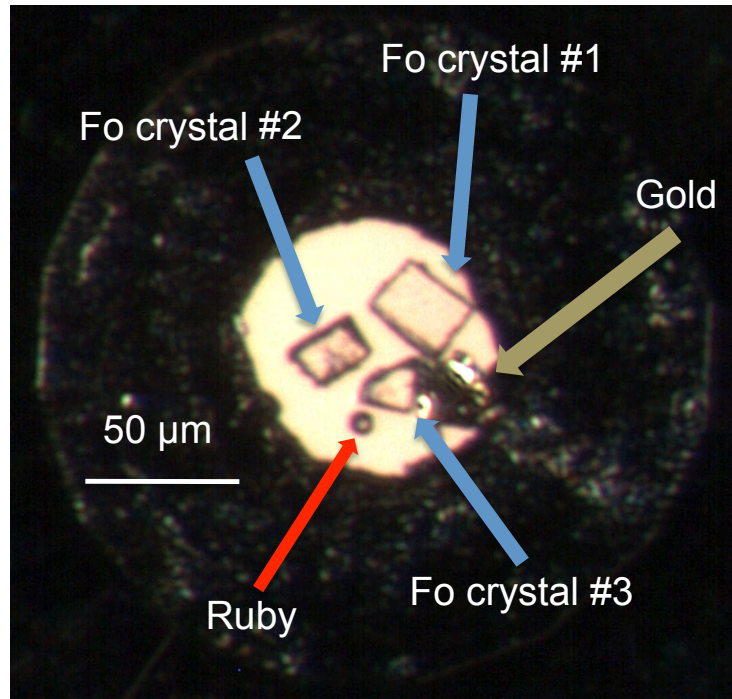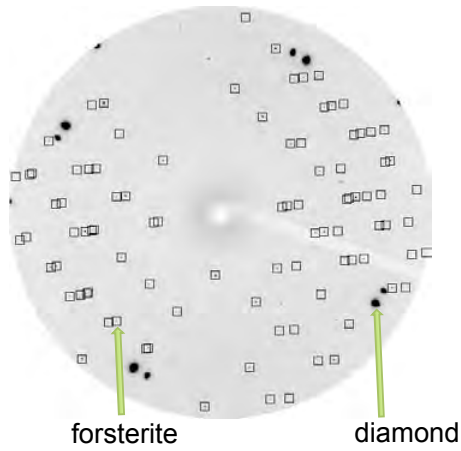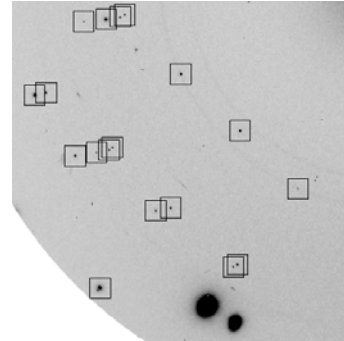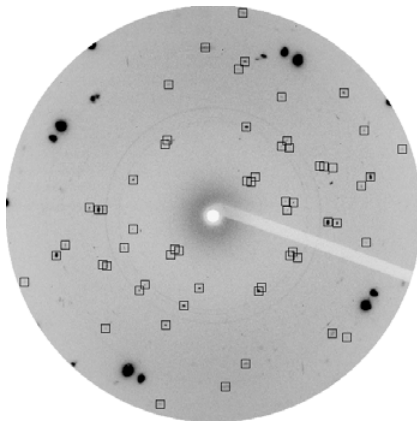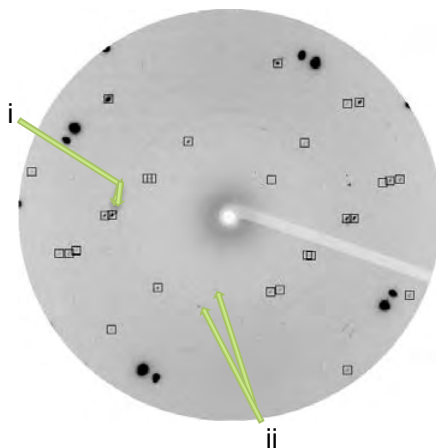| Atom	Wyckoff position	x/a	y/b	z/c
Mg1	4a	0.5	0.3636	0.3541
Mg2	4a	0.5	0.8861	0.6777
Si	4a	0	0.8720	0.0000
O1	4a	0.5	0.00466	0.4406
O2	4a	0.5	0.2537	0.5490
O3	4a	0.5	0.7048	0.3247
O4	4a	0.5	0.4526	0.1647

802

803

804

805

806

807

33

(a) Forsterite (48 GPa)

(b) Magnified Forsterite Diffraction

forsterite   diamond

(c) Forsterite II (52 GPa)

(d) Forsterite III (58 GPa)

(e) Magnified Forsterite III Diffraction

Mg pentagonal bipyramids and octahedra

Si tetrahedra and octahedra